H₂ VELOCITY STRUCTURE IN THE MOLECULAR OUTFLOW DR 21[1]

Irene Cruz-González,[2] Luis Salas,[3] and David Hiriart[3]

RESUMEN

Describimos la estructura en velocidad del chorro molecular DR 21 en la línea 2.12 μm del H₂. Se obtuvieron cubos de velocidad de la emisión total del chorro utilizando un interferómetro Fabry-Pérot de barrido con resolución espectral de 24 km s^{-1}. Se detectó emisión de H₂ de ambos lóbulos DR 21 (E) y DR 21 (W) en un intervalo de velocidad de $(-80.82, +46.84)$ km s^{-1}. Las regiones más conspicuas incluyen un chorro colimado y posiblemente su contra-chorro, una cavidad elíptica y cuatro estructuras en forma de arcos. El cubo de velocidad fué utilizado para calcular imágenes de los cuatro momentos de velocidad para estudiar los momentos a lo largo del eje del chorro molecular. Se estudia la turbulencia mediante un análisis de búsqueda de grumos. El estudio de las relaciones entre parámetros de los grumos y cinemáticos nos permitió derivar leyes de potencia en concordancia con las leyes de Larson.

ABSTRACT

We describe the velocity structure of the molecular outflow DR 21 in the 2.12 μm line of H₂. Velocity cubes were obtained of the entire outflow emission using a scanning IR Fabry-Pérot interferometer with a spectral resolution of 24 km s^{-1}. H₂ emission was detected from both the DR 21 (E) and DR 21 (W) lobes in a velocity interval $(-80.82, +46.84)$ km s^{-1}. The most conspicuous sources found include a jet-like region and a possible counter-jet or an independent jet, an elliptical cavity and four bow-like structures. The velocity data cube was used to calculate the four velocity moment images of the outflow to study the moments along the outflow axis. Turbulence in the outflow is studied via a Clump Find analysis. Relations between clump parameters and kinematics allowed us to derive power-law relations in agreement with Larson's laws.

Key Words: **ISM: INDIVIDUAL (DR 21) — ISM: JETS AND OUT-FLOWS — ISM: KINEMATICS AND DYNAMICS — ISM: MOLECULES — STARS: FORMATION**

1. INTRODUCTION

The compact H II region DR 21 is located on the southern end of the molecular cloud complex DR21-W75S. The molecular outflow DR 21 is centered on the H II region/molecular cloud core and is located at a distance of 2-3 kpc (Campbell et al. 1982). The distance to the source is quite uncertain and we adopt herein a value of 2.5 kpc. DR 21 is one of the largest (it extends over a projected distance of ∼5 pc on the sky), most massive ($>3000~M_\odot$) and most powerful ($> \times 10^{48}$ erg) outflows known in the galaxy (Garden et al. 1991a,b; Garden & Carlstrom 1992). The DR 21 outflow is oriented roughly E-W with a PA of 65° and it extends ∼6.5′on the sky.

The DR 21 outflow has been mapped in CO (Fischer et al. 1985; Garden et al. 1991b), vibrationally excited H₂ (Garden et al. 1986), $C^{18}O$ (Wilson & Mauersberger 1990), and HCO^+ (Garden & Carlstrom 1992). Evidence for high-velocity gas flow in DR 21 was first presented by Dickel, Dickel & Wilson (1978). In the lobes of the outflow the ^{12}CO J=1-0 and HCO^+ maps show a mixture of blue-shifted and

---

[1]Based on observations obtained at the Observatorio Astronómico Nacional at San Pedro Mártir, Baja California, México.

[2]Instituto de Astronomía, Universidad Nacional Autónoma de México, México, D. F., México.

[3]Instituto de Astronomía, Universidad Nacional Autónoma de México, Ensenada, B. C., México.

red-shifted emission, which favors the interpretation that the outflow lies very near to the plane of the sky.

The driving source of the outflow lies most probably near the location of the central peak of the HCO^+ emission shown in the map of Garden & Carlstrom (1992), at position RA(J2000.0) 203900.7, Dec(J2000.0) 421923.9. We will assume this as the position (0,0) of the driving source.

The eastern and western lobes of the outflow are separated by a dense molecular cloud detected in the NH_3 core by Wilson et al. (1995), which is thought to be a site of massive star formation, since it harbors several ultracompact H II regions (Harris 1973; Dickel et al. 1986; Cyganowski et al. 2003), an H_2O maser (Genzel & Downes 1977) and strong H I absorption (Roberts, Dickel, & Goss 1997). The continuum emission in the 6 cm map of Cyganowski et al. (2003) shows two cometary H II regions near the core of the DR 21 outflow.

The observed free-free emission of the associated H II regions requires several ionizing O stars according to Harris (1973). The spectral energy distribution from 1 to 1000 μm is presented in a far-infrared study of DR 21 by Colomé et al. (1995). The total integrated luminosity $L \sim 5 \times 10^5 L_\odot$ (Campbell et al. 1982) responsible for ionization and dust heating requires a central O6 star.

Marston et al. (2004) present IRAC images obtained with the Spitzer Space Telescope covering ~ 0.5 deg^2 of the region W75/DR 21. They show that the molecular outflow clearly stands out in the 4.5 μm wave-band of IRAC, which encompasses atomic and molecular emission lines that are excited only in hot gas, including rovibrational CO v =1-0 at 4.45–4.95 μm, the H_2 0–1 S(9) line at 4.694 μm and the H I Brα line at 4.052 μm. The outflow driving source position is not presented since these authors detected several heavily obscured candidates.

In this paper a scanning IR Fabry-Pérot interferometer was used to obtain velocity cubes of the DR 21 outflow in the emission line of H_2 v=1-0 S(1) 2.12 μm. Detailed kinematics of both the DR 21 (E) abd DR 21 (W) lobes are studied using position-velocity diagrams and the four velocity moment images. Turbulence in the DR 21 outflow is studied via a statistical approach using a Clump Find algorithm.

2. OBSERVATIONS

2.1. *Molecular hydrogen scanning Fabry-Pérot observations*

The molecular hydrogen scanning Fabry-Pérot observations of DR 21 were carried out on 1998 October 5 at the 2.1-m telescope of the Observatorio Astronómico Nacional at San Pedro Mártir (Baja California, México). The measurements were obtained with the CAMILA near-infrared camera/spectrograph (Cruz-González et al. 1994) and the addition of a Queensgate Fabry-Pérot interferometer, positioned in the collimated beam of the cooled optical bench. A detailed description of the near-IR scanning Fabry-Pérot instrumental setup is presented by Salas et al. (1999).

The Fabry-Pérot setup has a spectral resolution of 24 km s^{-1}; to restrict the spectral range for the H_2 v=1-0 S(1) line emission an interference filter (2.122 μm, $\Delta\lambda$=0.02 μm) is required. The bandwidth of this particular filter allows 11 orders of interference. Only one of these orders contains the H_2 2.122 μm line, while the remaining orders contribute to the observed continuum. The spatial resolution of the instrumental array is 0.86″pixel^{-1} which yields a field of view of 3.67′× 3.67′.

The CAMILA field of view (3.67′ × 3.67′) and the extent of the outflow compelled us to take a set of images for the western region of DR 21 and another set for the eastern one. The region of the molecular outflow DR 21 covered is 7.0′× 4.6′, which corresponds to 5.1 pc × 3.4 pc at the adopted distance of 2.5 kpc.

Images of each region of interest were obtained at 26 etalon positions, corresponding to increments of 9.82 km s^{-1}. The observing sequence consists of tuning the etalon to a new position and imaging the source, followed by a sky exposure at an offset of 3′ to the north (RA(J2000.0) 203855.8, Dec(J2000.0) 422208). A bright star at position (163,160) in both east and west frames invalidates a region of 5 pixels in every frame. The telescope allowed the on-source image to be accurately positioned back within 1″, eliminating re-centering problems. The integration time of 60 s per frame was short enough to cancel the atmospheric line variations at each etalon position, but long enough to obtain a good signal-to-noise ratio (S/N). The typical 1σ noise in any image is 0.13 counts s^{-1} pixel^{-1}, while the intensity in extended emission regions of interest goes up to 1 counts s^{-1} pixel^{-1}. For spectral calibration the line 2.1332885 μm of the argon lamp was observed at each etalon position, yielding a velocity uncertainty of 1 km s^{-1} in the wavelength fit. The instrumental response was observed to be Lorentzian, with a FWHM of 2.4 channels.

A set of high- and low-illumination sky flats was obtained at sunset for flat-fielding purposes. Images

under photometric conditions were taken on October 5, 1998, with a FWHM of 1.9″.

2.2. *Velocity calibrated cubes*

We reduced the data to obtain the velocity calibrated channel images using the software and the data reduction technique employed for the Orion BN-KL region and described in Salas et al. (1999). We calculated LSR velocities for each channel as

$$v_c = (channel - can0)\Delta(v) + v_{LSR} \quad , \quad (1)$$

where $can0$=13.88 is the channel where the H$_2$ 2.12 μm line is at rest in the observer frame; v_{LSR}=6.38 km s^{-1} is the radial velocity correction for the DR 21 region at the time of observation, and $\Delta(v)$=9.82 km s^{-1}.

To increase the signal to noise (S/N), at the expense of lowering the resolution, we filtered each channel image in the following way: First, we ran a median filter with a 3×3 window to get rid of spikes. Stars or unresolved sources are not affected by this filter since the FWHM of observations is 2.2 pixels larger than the features that are removed. Next, a 1.5 sigma Gaussian was convolved with each channel image. This reduced the noise level to 0.02 counts s^{-1} pixel^{-1}, therefore increasing the S/N ratio by a factor of 6.5. However, the FWHM was increased to 3.9″, a factor of two loss in angular resolution. We felt that the gain in S/N was worth the price.

The plate scale solution was obtained using 4 stars from the HST guide star catalog or the 2MASS survey to reference each of our regions (east and west independently). The plate was solved with a first degree polynomial in each direction, with scale, centering and rotation, to an accuracy of 1″.

3. RESULTS

3.1. *H$_2$ velocity maps*

The DR 21 molecular cloud rest velocity v_{LSR} is -2.5 km s^{-1} according to Garden et al. (1991b) and Garden & Carlstrom (1992).

Velocity channel images were individually obtained for DR 21 (E) and DR 21 (W) from the position-velocity cube data. For each pixel on the image, we subtracted a continuum intensity level calculated from the median of the channels with no emission. H$_2$ v=1-0 S(1) 2.12 μm line emission of the outflow DR 21 was detected in velocity channels -80.82 km s^{-1} to $+46.84$ km s^{-1} in DR 21. The two sets of maps were pasted together to create velocity channel maps of the complete region. Figure 1 shows six of these maps (channels 10 to 15) covering

local standard of rest (LSR) velocities from -31.72 to $+17.38$ km s^{-1}.

The DR 21 outflow is extremely clumpy and shows considerable structure. The most conspicuous H$_2$ emission structures in DR 21 (E) are a filament A, designated DR 21 (E):A, that ends in the eastern tip of the outflow and a large arc or bow-like structure B, DR 21 (E):B. Whereas in DR 21 (W) the emission is split into four regions C to F (Figure 1), near the central region of the outflow a faint clump is seen, C, DR 21 (W):C, elongated N-S, as well as two bow-like clouds D and E, DR 21 (W):D and DR 21 (W):E, a sharper one F, DR 21 (W):F, at the western-most region which delineates the tip of the outflow. These three H$_2$ bow structures converge to the apex of the outflow. We note that clump C is detected in all channels, probably indicating that the continuum of a reflection nebulosity is observed.

The H$_2$ outflow extends on the sky over $\sim$6.5′, which corresponds to a projected distance of 4.7 pc at D=2.5 kpc.

3.2. *Color Doppler images*

A color-coded Doppler image from the six channel velocity maps with stronger emission corresponding to LSR velocities is presented in Figure 2 (top). Blue runs from -31.72 to -21.90 km s^{-1} (channels 10 and 11), green from -12.08 to -2.6 km s^{-1} (channels 12 and 13) and red from $+7.56$ to $+17.38$ km s^{-1} (channels 14 and 15). Since the molecular cloud rest velocity v_{LSR} is -2.5 km s^{-1}, the green color indicates gas close to the rest velocity. We have also marked the most conspicuous structures A to F noted in Figure 1 and described above. The velocity structure in both regions shows a very complex clumpy pattern. DR 21 (E) is dominated by the blue and green velocity components and red velocities appear only at the tip of the lobe. The C cloud above the driving source seems dominated by the continuum (maybe it is a reflection nebulosity rather than a shocked region). DR 21 (W) shows a complex velocity field, the first bow D is blue (-31.72 to -21.90 km s^{-1}), the second E is red ($+7.56$ to $+17.38$ km s^{-1}) while the third F is greenish (-12.08 to -2.6 km s^{-1}). The western lobe converges to the apices of the three bow structures observed.

We note that the two inner bows, B on the east and D on the west seem to describe the edges of an elliptical cavity. However, the western edge is bluer, indicating a possible inclination effect. Although the cavity border is not seen complete, the major and minor axes of this cavity are estimated to be 1.8 pc and 0.8 pc, respectively. Inside the cavity the detection
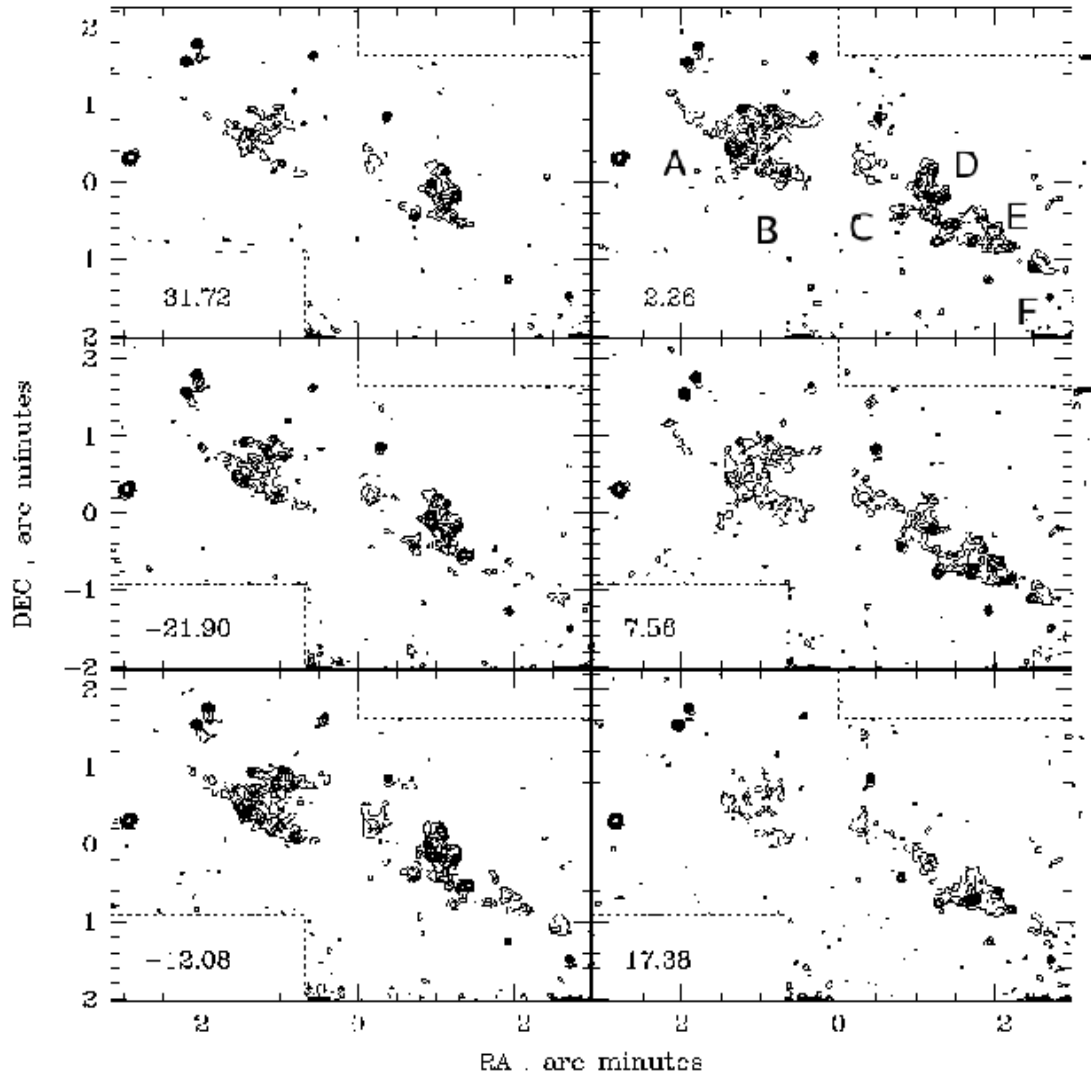
Fig. 1. Velocity channel maps of the H_2 v=1-0 S(1) line emission in DR 21, showing the radial velocity structure of the two regions DR 21 (E) and DR 21 (W). The velocity varies from -31.72 km s^{-1} in channel 10 (top left) to $+17.38$ km s^{-1} in channel 15 (bottom right), and the channel width is 9.8 km s^{-1}. The minimum contour level is 0.12 counts s^{-1} and the incremental values are 0.12 counts s^{-1}. Regions with no observed data are marked by a dotted rectangle. The (0,0) position corresponds to that of the HCO$^+$ peak at RA(J2000.0) 203900.7, Dec(J2000.0) 421923.9 (Garden & Carlstrom 1992). Offsets are referred to this position.

of H_2 is limited to a few small low surface brightness clumps near structure C, so most of the H_2 gas has been swept out by the outflow.

A blue jet-like structure is quite evident in Figure 2 since it lies at the center of the bow B but moves faster. We propose that this is indeed a jet based on the following arguments: (i) It has a filamentary structure extending for at least 64″(0.73 pc at 2.5 kpc) with a width of 6″; (ii) the kinematics of the jet is quite different from that of the surrounding cloud (B); indeed $v_j = -18 \pm 5$ km s^{-1} while $v_B =$ -9 ± 5 km s^{-1}; (iii) the jet is well aligned with the outflow driving source and with the eastern tip of the outflow (A); (iv) the jet speed is the fastest region found in DR 21 (E); and (v) the jet is centered inside the cavity described by region B.

In the bottom panel of Figure 2 we modified the velocity intervals for each color. Blue now runs from -51.36 to -41.54 km s^{-1}, green from -31.72 to -21.90 km s^{-1}, and red from -12.08 to -2.6 km s^{-1}. In DR 21 (W) we note a faint structure that could be the counter-jet to the south of the structures D
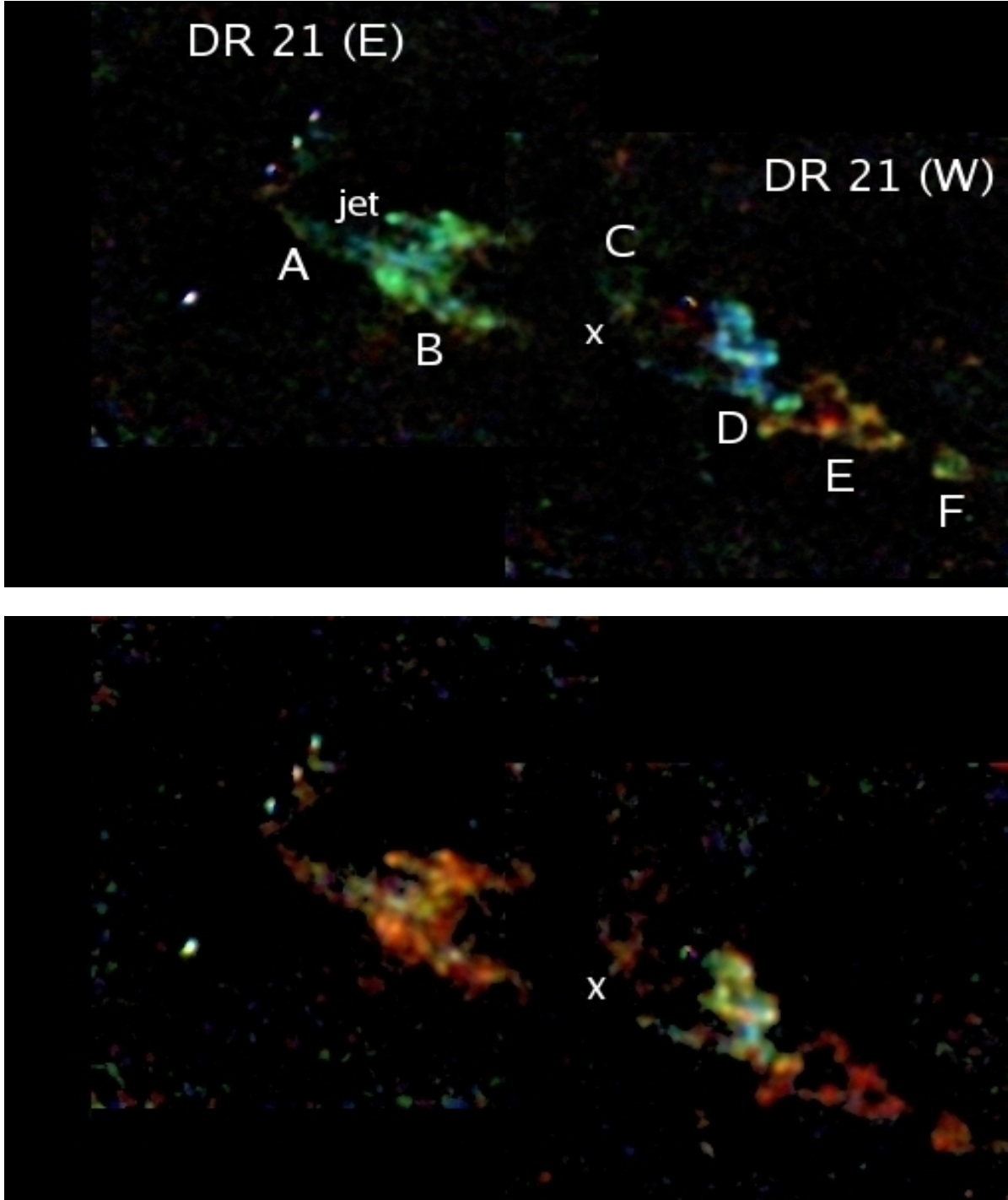
Fig. 2. Color composite of the Doppler-shifted H$_2$ v=1-0 S(1) 2.12 μm line emission in the outflow DR 21. Top: Image color corresponding to LSR velocities: blue -31.72 to -21.90 km s^{-1}, green -12.08 to -2.6 km s^{-1}, and red $+7.56$ to $+17.38$ km s^{-1}. Bottom: Image color corresponding to LSR velocities: blue -51.36 to -41.54 km s^{-1}, green -31.72 to -21.90 km s^{-1}, and red -12.08 to -2.6 km s^{-1}. The driving source adopted position is marked by **X**. Labels **A** to **F** are defined in the text. The region shown is about $7.0' \times 4.6'$ (5.1 pc $\times$ 3.4 pc at distance D=2.5 kpc). The outflow extends on the sky $\approx 6.5'$ which corresponds to a projected distance of 4.7 pc. North is at the top and east is to the left.
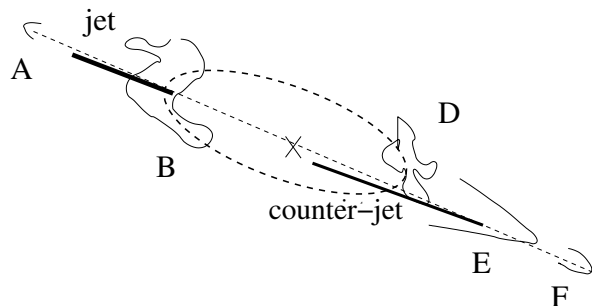
Fig. 3. Schematic diagram of the observed structures.

and E. Arguments in favor of a counter-jet are: (i) it is roughly aligned with the eastern jet; (ii) it is aligned with the driving source and with the apices of bow structures E and F; (iii) $v_{cj} = -25 \pm 7$ km s^{-1} is smaller than those of the nearby clouds $v_{E,F}$ (+5 $\pm$ 5 and 0 $\pm$ 5 km s^{-1}, respectively). However, arguments against the presence of a counter-jet are: (i) the counter-jet is bluer than the jet by 10 km s^{-1} and should be redder than the central velocity, (ii) the complexity of structure D which extends to the north and shows a rather complex velocity field, and (iii) the observed intensity is just above our detection limit (S/N∼5). The kinematics favor the presence of two independent jet-like structures.

For clarity we show a schematic view of all these elements in Figure 3. The line traced goes from the tips of the bow shock structures in DR 21 (W) across the HCO$^+$ peak; the line crosses the internal jet and ends at the tip of the eastern lobe.

Finally, the complex structure of the DR 21 outflows, including several clumps of molecular gas emission with different velocities, suggests that a statistical analysis might be useful. This approach is carried out in the following sections.

4. EXCITING SOURCE

The location and identification of the outflow central source is still uncertain. Garden & Carlstrom (1992) favor the central source at RA(J2000.0) 203900.7, Dec(J2000.0) 421923.9, the position of the HCO$^+$ molecular peak. The presence of the internal jet-like blue-shifted structure in the eastern lobe described above, as well as the possible counter-jet, strongly favor this position. Dust extinction is quite high in the central region of the outflow, as is shown in the images of Davis & Smith (1996), and precludes its direct observation in the infrared. The eastern cavity of the outflow is filled by two cometary H II regions (observed by Cyganowski et al. 2003) that occupy the empty region between
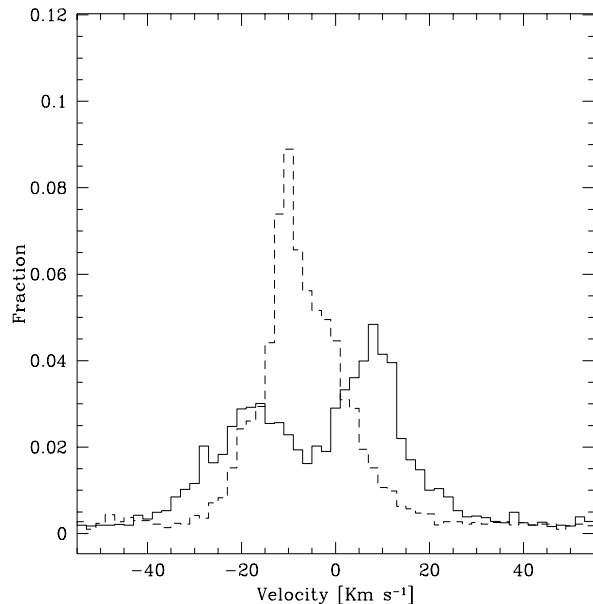

Fig. 4. Fraction of pixels with a given value of the centroid radial velocity (LSR) for DR 21 (E) (dashed line) and DR 21 (W) (solid line). The size of the bins is 2 km s^{-1}.

the HCO$^+$ peak and component B (see their Figure 1) shows the 6 cm continuum emission. If their map is superimposed on the H$_2$ image the dominant H II region cometary axis aligns quite well with the eastern part of the infrared jet. The kinematics of the hydrogen recombination lines at H66α and H53α reported by Cyganowski et al. (2003) show line widths of ∼30 km s^{-1} and LSR peak velocities between +6 and −4 km s^{-1}.

5. OUTFLOW KINEMATICS

5.1. Centroid radial velocity

We have calculated the centroid radial velocity for each pixel by taking only 10 velocity channels around the peak intensity. Figure 4 presents histograms of centroid radial velocity for the two H$_2$ emission regions. DR 21 (W) shows a bimodal radial velocity distribution with peak velocities of +10 km s^{-1} and −17 km s^{-1}. The reddest component arises mainly from clouds E and F. DR 21 (E) shows a single peak at velocity of about −10 km s^{-1} which extends asymmetrically towards the red. The H$_2$ peak velocities of DR 21 (E) are quite consistent with the H66α peak velocities between +6 and −4 km s^{-1} reported by Cyganowski et al. (2003). The observed velocity fields in H II support their conclusion that the observed cometary morphologies are produced by bow shocks. The similarity of
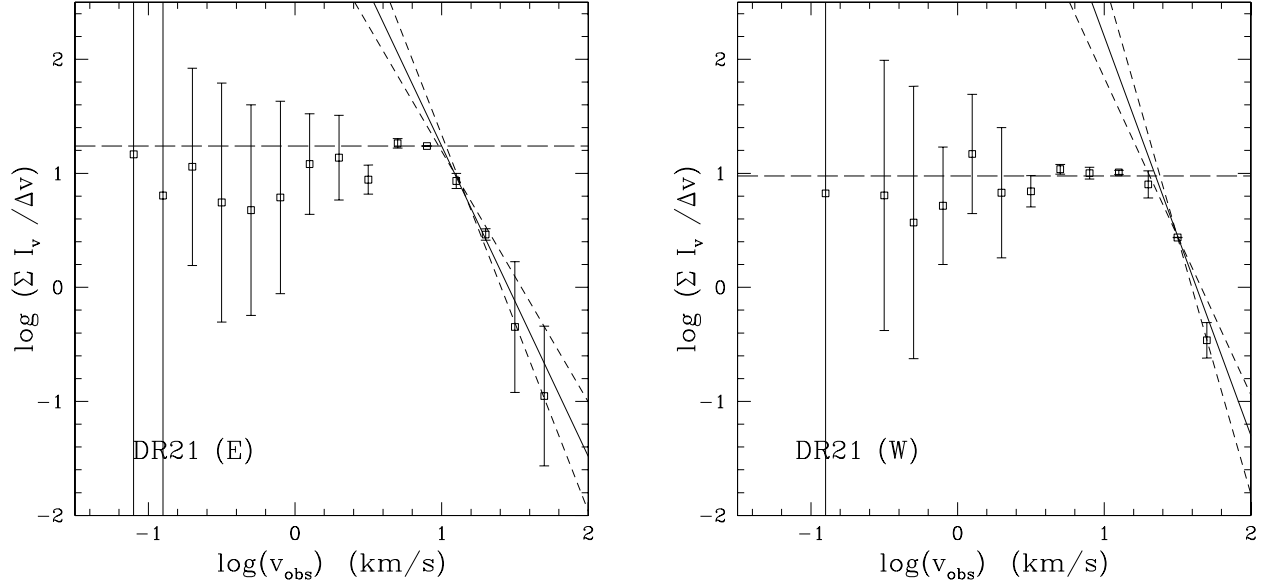
Fig. 5. Flux-velocity relation of $H_2 S(1)$ v=1-0 S(1) emission in DR 21 (E) (left) and DR 21 (W) (right). The long-dashed line shows the flat low velocity behavior up to a break velocity, whereas the solid line indicates a power-law decrease. The short-dashed lines show the range of possible values of the power-law index, 2.7±0.55 for DR 21 (E) and 3.5±0.9 for DR 21 (W), and of $\log(v_{break})$ (1.00±0.03 and 1.35±0.03, respectively).

H_2 and H II kinematics and the morphology match between the eastern infrared jet and the dominant H II region cometary axis strengthen the bow shock model plausibility.

5.2. *Flux–velocity relation*

We have calculated the flux-velocity diagrams for the individual DR 21 (E) and DR 21 (W) lobes, as described in Salas & Cruz-González (2002). For every pixel with signal above the detection threshold, we added the fluxes of all the pixels with centroid velocities in bins of observed centroid velocity $|v_{obs} - v_{rest}|$, with respect to the rest velocity of the region (-2.5 km s^{-1}). The flux-velocity diagrams for DR 21 so obtained are shown in Figure 5. As shown by Salas & Cruz-González (2002), this procedure gives similar flux-velocity relations for a variety of outflows, consisting of a flat spectrum for low velocities followed by a power-law decrease

$$\frac{dF}{dv} \propto v^{\gamma} \qquad (2)$$

above a certain break velocity. This power-law is also found in CO outflows (Yu, Billawala, & Bally 1999). The power-law index is very similar for different outflows, as is the case for DR 21 (E) and DR 21 (W), in which γ is 2.7±0.6 and 3.5±0.9, respectively (Figure 5, solid lines). The break velocity,

however, is slightly different. The logarithm of v_{break} (in km s^{-1}) takes values of 1.00±0.03 and 1.35±0.03, respectively, which suggests that v_{break} may be twice as large for DR 21 (W). As was discussed in Salas & Cruz-González (2002), outflows of different lengths (l) show break velocities varying as $v_{break} \propto l^{0.4}$. This could be due to an evolutionary effect. However, in the case of DR 21 (E) and DR 21 (W) the lobe length is very similar, as might be the age. Salas & Cruz-González also argue that another cause for a difference in break velocities could be the amount of turbulence in the outflow, which might be the case for DR 21. Turbulence in the DR 21 outflow is discussed in § 7.

5.3. *Position-velocity diagrams*

Figure 6 presents the centroid radial velocity as a function of displacement along the right ascension axis for both DR 21 (E) and DR 21 (W). All the channels with detected H_2 emission are shown. The radial velocity in DR 21 (E) appears dominated by a gradient from $+5$ km s^{-1} to -15 km s^{-1}, as if it were accelerating (Hubble flow), followed by a steeper deceleration. In DR 21 (W) we note two different systems. First, there is a cloud D with a wide range of blue velocities from -10 to -35 km s^{-1}. Second, the outflow abruptly becomes red-shifted, and bows E and F have velocities around $+8$ and $+5$ km s^{-1}, respectively.
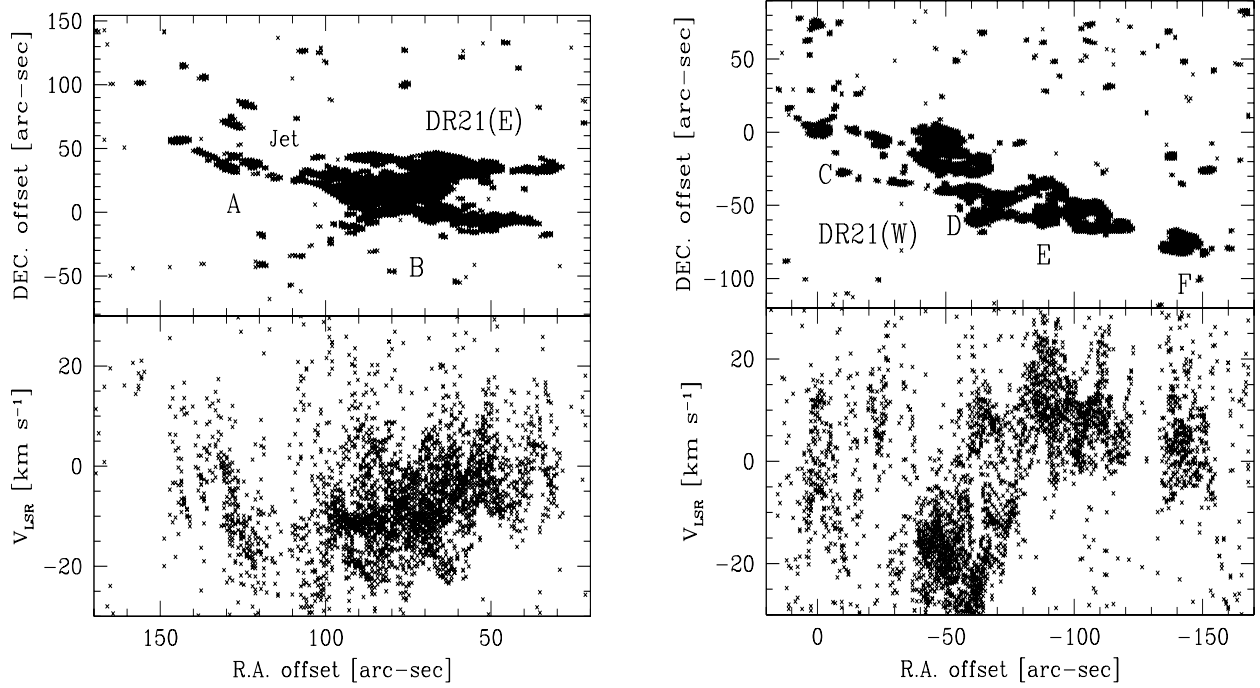
Fig. 6. Diagrams of detected H_2 v=1-0 S(1) line emission in all velocity channels (top) and the velocity-position diagrams (bottom) for DR 21 (E) (left) and DR 21 (W) (right). Offset values are referred to the position (0,0) of the driving source (HCO^+ peak; Garden & Carlstrom 1992).

5.4. *Velocity moments*

To study the kinematics of the region quantitatively, we have calculated the first four moments of the intensity-velocity distribution. We have used for this purpose the median filtered, Gaussian convolved images. For each pixel in the images, we subtract a continuum defined as the median of the 19 lowest intensity channels. Next, we evaluate the signal peak above this continuum. To be considered validated, a pixel must have a peak intensity of 5 sigma above the continuum. Then, the four first moments are evaluated. To evaluate these integrals we only considered 5 channels to each side of the peak intensity channel. This is mainly intended to limit the value of the second moment integral, which is known to diverge for a Lorentzian function.

It may be easily shown that the square root of the second moment of this function is

$$ s \sqrt{\frac{2}{\pi}\left[\frac{l}{s} - \tan^{-1}\left(\frac{l}{s}\right)\right]} \quad , \qquad (3) $$

where $2s$ is the FHWM of the Lorentzian and l (=5 channels) defines the limits of the moment integral (peak $-l$ to peak $+l$). The square root of the second moment takes the value of 15.82 km s^{-1} for the

present parameters, indicating that such a value of the square root of the second moment is expected from purely instrumental and reduction related parameters. Values of the square root of the second moment in excess of this would represent real velocity dispersions.

We have used the velocity data cube to calculate the four velocity moment images of the DR 21 outflow. This data were used to average the observed moments along each outflow lobe, assuming that the center is located at the position of the exciting source (see § 4) and that the outflow has a PA=66°. We took averages along a slit of 120 pixels ($\pm$ 60 pixels) from the proposed outflow axis.

The four velocity moments along the outflow lobes are presented in Figure 7 for DR 21 (E) and DR 21 (W). From bottom to top are shown intensity, centroid velocity referred to the LSR, velocity dispersion and kurtosis. The error bars are standard deviations from the mean.

For DR 21 (E) the intensity shows three peaks at 45″ (0.55 pc at D=2.5 kpc), 95″ (1.15 pc) maximum of cloud B, and 160 ″ (1.94 pc) apex of bow A. For DR 21 (W) three peaks are evident at 65″ (0.8 pc), 130″ (1.6 pc), and 165″ (2.0 pc), corresponding to structures D, E and F.
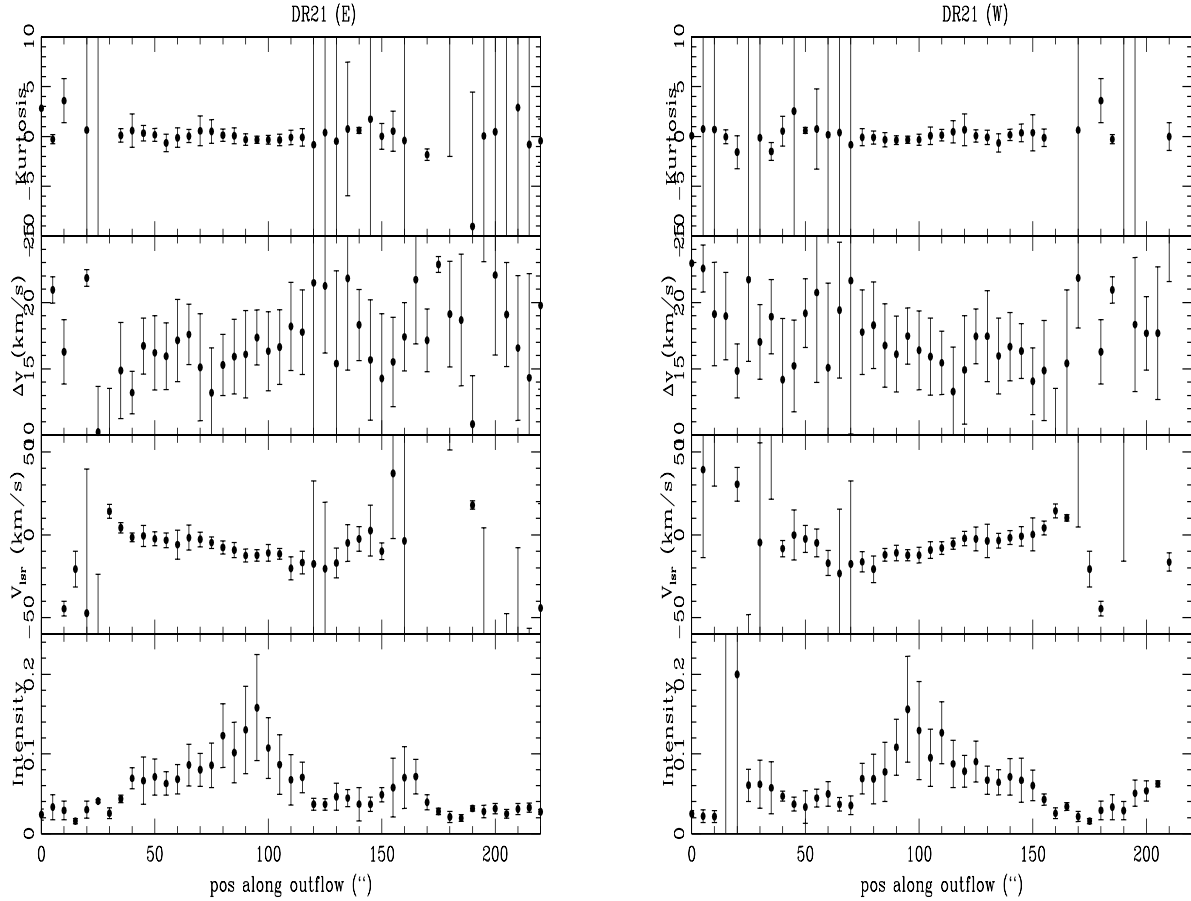
Fig. 7. Velocity moments along the outflow DR 21 (E), from bottom to top: intensity, centroid velocity, velocity dispersion and kurtosis for DR 21 (E) (left) and DR 21 (W) (right).

Velocity gradients in DR 21(E) are seen from $+13$ to -20 km s^{-1} in the region from $30''$ to $110''$, in agreement with the description presented in § 3.2. DR 21 (W) shows blue-shifted velocity -20 km s^{-1} from $40''$ to $70''$, corresponding to part of the D structure followed by the redshifted bows E and F. The velocity dispersion for DR 21 (E) shows an increasing gradient in the region of structure B. For clouds D and E of DR 21 (W) similar gradients are observed. This effect is possibly produced by increasing turbulence upstream in the outflow.

The kurtosis is 0 within the error bars, indicating mostly symmetrical lines within the averaged slit regions.

6. CLUMP ANALYSIS

We have used the Clump Find Algorithm presented by Williams, de Geuss, & Blitz (1994) to locate 3-D coherent structures (clumps) in the data cubes. The median-Gaussian filtered images were used for this and further analysis. Following their suggestion, we set the contour level increment to 2σ (0.04 counts s^{-1} pixel^{-1}) and we are even more restrictive on the floor level, setting it to 6σ to avoid mistaken identification as signal of low-level coherent noise, resulting from the filtering process.

With these parameters we were able to detect about 200 clumps at each of the outflow lobes. The clump analysis yields the area and location of each clump.

The area of each clump along the outflow lobes is shown in the bottom panel of Figure 8. Note that we assumed the same position of the central source and outflow PA described above in § 5.4. Near the center of DR 21 (E) the clump areas are small, at $\approx 50''$ their value increases and reaches a maximum at $\approx 80''$, which coincides with the main bow structure in this lobe; they decline beyond this region and reach small values at the apex of the lobe. For DR 21
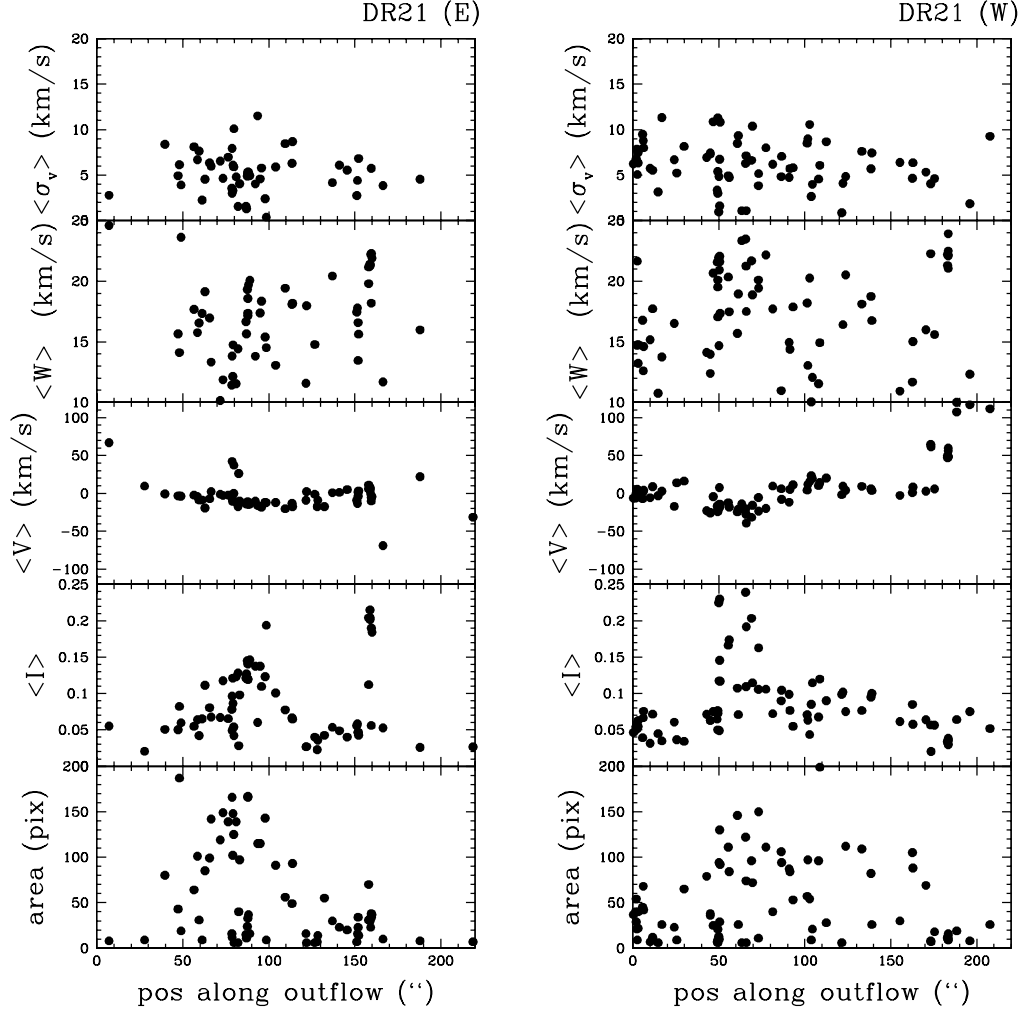
Fig. 8. Clump area and clump velocity moments along the outflow for DR 21. Each point on the graphs represents an identified clump along the outflow. From bottom to top the graphs present the area, intensity, centroid velocity, line width $< W >$, velocity dispersion σ_v for each clump of DR 21 (E) (left) and DR 21 (W) (right).

(W) clump areas show a similar behavior; first they rise and near the bow regions they reach maximum sizes; they decline beyond the bow. Clumps of small areas are also evident at all positions along the outflow lobes.

Next, we looked for representative values of the velocity moments for each clump. In doing this, we depart from the moments calculated in the previous section, I, V_c and W for the order 0, 1 and 2 moments, and compute the following spatial averages (c.f. Riera et al. 2003; Hiriart, Salas, & Cruz-González 2004):

$$\langle I \rangle = \frac{\int_{v_i} \int_{S_i} I(x',y')dx'dy'dv}{\int_{v_i} \int_{S_i} I(x',y')dx'dy'dv} , \qquad (4)$$

$$\langle V_c \rangle = \frac{\int_{v_i} \int_{S_i} V_c(x',y')I(x',y')dx'dy'dv}{\int_{v_i} \int_{S_i} I(x',y')dx'dy'dv} , (5)$$

$$\langle W^2 \rangle = \frac{\int_{v_i} \int_{S_i} W^2(x',y')I(x',y')dx'dy'dv}{\int_{v_i} \int_{S_i} I(x',y')dx'dy'dv} ,(6)$$

and

$$\langle \sigma_v{}^2 \rangle = \frac{\int_{v_i} \int_{S_i} [V_c(x',y') - \langle V_c \rangle]^2 I(x',y')dx'dy'dv}{\int_{v_i} \int_{S_i} I(x',y')dx'dy'dv} . \qquad (7)$$

Note that these integrals are carried out over velocity intervals v_i and areas S_i that correspond to each identified clump.

The Clump Find analysis delivers velocity information for each clump found. These data allow us

to construct moment vs. position-along-the-outflow diagrams, assuming the same position of the central source and outflow PA as described in § 5.4.

The diagram of the intensity for each clump along the outflow (Figure 8 second panel from bottom to top) shows that we recover the peaks associated to the bow shock structures discussed above. The dispersion in this case is larger and the peaks are not as clearly defined as in Figure 7.

The centroid velocity gradients (Figure 8 third panel from bottom to top) are here more evident. For DR 21 (E) the velocity decreases from the center to about $70''$, remains flat and increases beyond $\sim 110''$. For DR 21 (W) the velocity becomes redshifted beyond $90''$.

The clump analysis results are quite consistent with the velocity moment analysis presented in the previous section. This is also true for the next panel in Figure 8, the line width or line velocity dispersion $< W >$. The top panel shows a newly introduced variable, σ_v, the velocity dispersion within each clump. For DR 21 (E) σ_v is around 5 ± 3 km s^{-1} and has no strong variation with position along the outflow. For DR 21 (W) slightly higher values 6 ± 3 are observed (see Figure 8).

7. CLUMP PARAMETERS AND KINEMATICS ANALYSIS

7.1. $\sigma_v \propto R^a$

We can examine the variations of the observed σ_v velocity dispersion with the characteristic length R of the clump

$$\sigma_v \propto R^a \quad . \tag{8}$$

We want to compare them with the first Larson's law $a=0.38$ for molecular clouds (Larson 1981) and with the different possible values of the power index a, ranging from $1/3$ for pure Kolmogorov turbulence to 0.5, a more suitable value for virial equilibrium (e.g., Goodman et al. 1998).

Figure 9 top panel shows σ_v as a function of clump area ($A \propto R^2$). Also shown are the relations expected for the virial equilibrium ($a=0.5$) and Kolmogorov ($a=0.33$) cases. Considering all the clumps in each lobe the correlation is weak. A better result is obtained for clumps in some of the individual H$_2$ clouds, as is shown in the bottom panels. Cloud B in DR 21 (E) shows a spectral index of $a =0.31\pm0.11$ (with correlation coefficient $r=0.43$). A better correlation ($r=0.64$) is obtained for cloud D in DR 21 (W), with a spectral index $a=0.62\pm0.16$.

This last result indicates that the eastern outflow is most likely fully turbulent, while the western one seems more virialized. Thus, we present evidence

that supports a differentiated kinematics for each lobe. This result agrees with Davis & Smith (1996) finding that the northeastern lobe H$_2$ profiles favor a fully turbulent lobe while the western lobe profiles are produced by resolved structures. The differentiated kinematics of the lobes in DR 21 is similar to our finding in the Cep A H$_2$ outflow (Hiriart, Salas, & Cruz-González 2004).

7.2. $\sigma_v \propto I^c$

Another power-law relation obtained for OH, C^{18}O and NH$_3$ maps in dense cores of molecular clouds (described by Goodman et al. 1998), is line width vs. antenna temperature T_A. In the case of H$_2$ mapping the equivalent to this relation would be velocity dispersion vs. intensity.

To explore this possibility in the DR 21 outflows, Figure 10 shows the variation of clump velocity dispersion σ_v with intensity I. As is shown in both lobes of DR 21 the σ_v–I relation can be described by a power-law

$$\sigma_v \propto I^c \quad , \tag{9}$$

where large σ_v values correspond to fainter sources. DR 21 (E) shows that a single steep power-law $c = -1.33 \pm 0.15$ describes the variation, while a shallower slope $c = -0.92 \pm 0.15$ is found in DR 21 (W).

7.3. Second Larson's Law: $n \propto R^{-1.1}$

We explore the second Larson's law, density vs. cloud size,

$$n \propto R^b \tag{10}$$

with b≈ -1.1 for molecular clouds (Larson 1981).

If the emission is optically thin, the column density $N \propto \int I_v dv$. In a region with single line profiles (Gaussian or other) we can approximate the integral and obtain $N \propto I_v \sigma_v$, because σ_v dominates the line width Δv.

Substituting the two previous power-laws given in Equations 8 and 9 we obtain

$$N \propto R^{a(1+1/c)} \quad . \tag{11}$$

Finally, if we assume that the line of sight clump size is similar to the characteristic length in the plane of the sky, then $n = N/R$ and

$$n \propto R^{a(1+1/c)-1} \tag{12}$$

so $n \propto R^b$ with $b = a(1 + 1/c) - 1$.

For H$_2$ gas in the DR 21 outflow we obtain that b is -0.92 ± 0.19 for DR 21 (E) and -1.05 ± 0.22 for DR 21 (W), respectively. We conclude that both
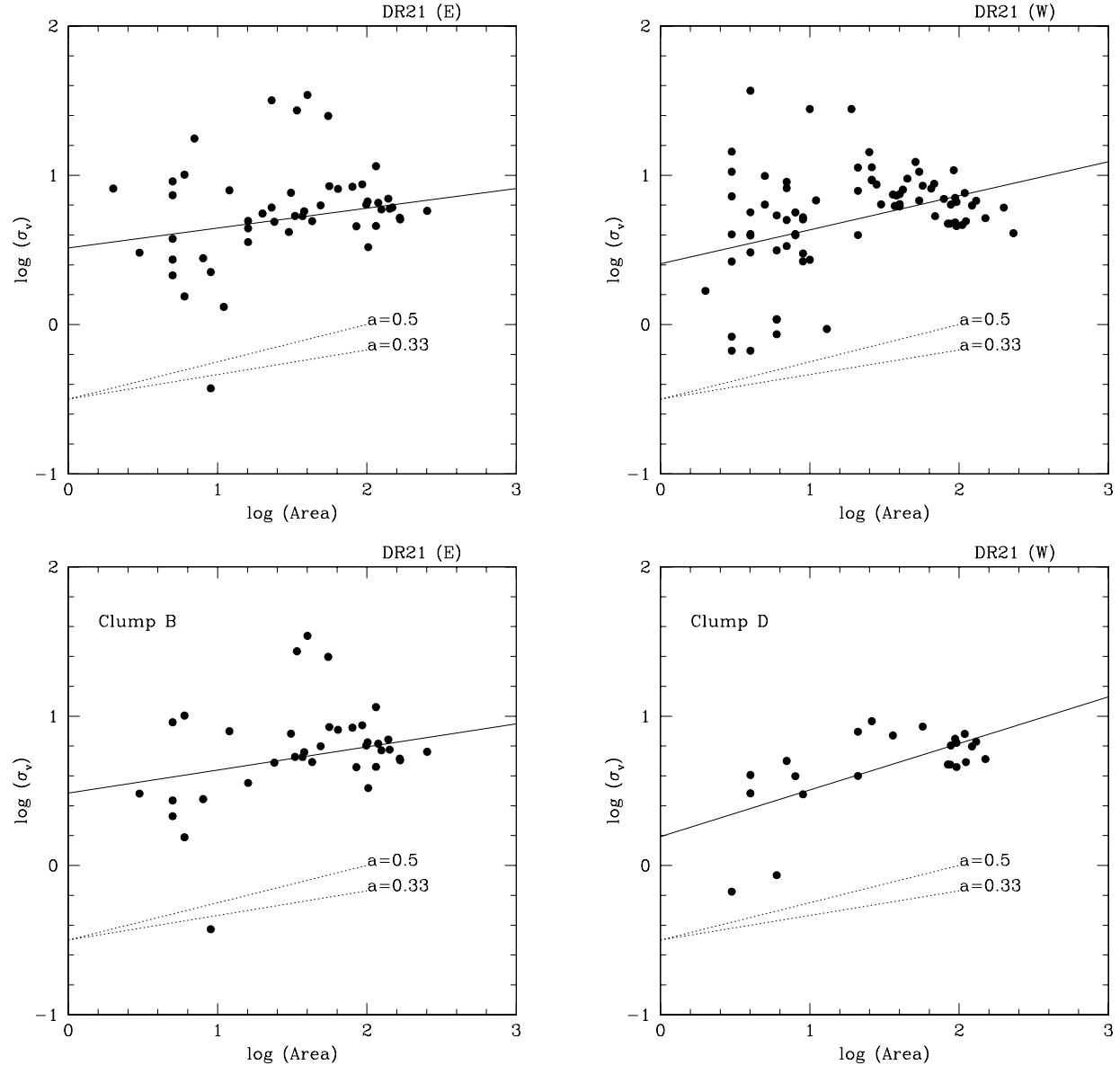
Fig. 9. Clump velocity dispersion σ_v vs. clump area for DR 21 (E) (left) and DR 21 (W) (right). Clumps B in DR 21 (E) (left) and D in DR 21 (W) (right) are shown in the bottom panels. In all the panels a solid line represents a linear least-square fit to the data. The two line segments below are the representative power-law indices corresponding to slope a values of 0.33 for a Kolmogorov turbulence and 0.5 for a more virialized gas.

lobes yield b values quite consistent with Larson's second law value b of -1.1 and as Goodman et al. (1998) point out, close to the virial equilibrium value of -1 (virialized values $b = -1$ and $a = 0.5$).

7.4. Summary

As mentioned in § 5.2 differentiated turbulence of the outflow lobes could be the source of the observed differences in break velocity in the flux-velocity relation (see Equation 2). In the current section we have discussed the differentiated kinematical regimes of each lobe in the DR 21 outflow, which lead us to conclude that indeed v_{break} may be related to turbulence in the molecular gas.

A summary of the four power-law relations (Equations 2, 8, 9, and 10) between kinematic parameters (flux, velocity) and clump properties (size, intensity, clump velocity dispersion, density) of the DR 21 outflow obtained in this paper is presented in Table 1.
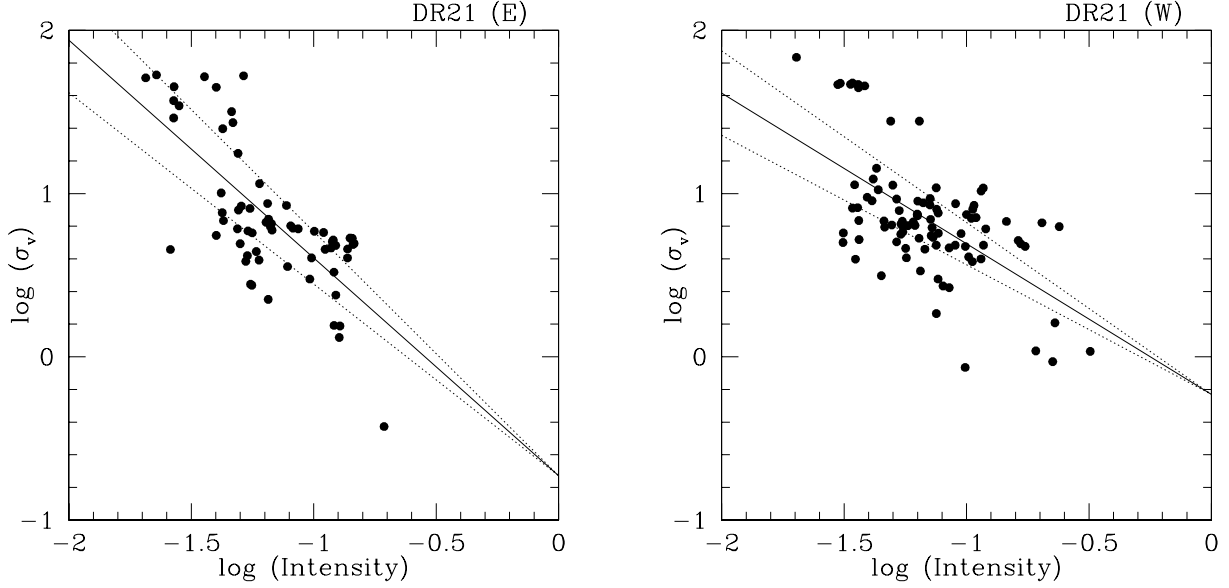
Fig. 10. The clump velocity dispersion σ_v vs. intensity I shows a power-law $\sigma_v \propto I^c$, where a large σ_v corresponds to fainter sources. DR 21 (E) is on the left and DR 21 (W) is on the right. The linear fit for each lobe is shown as a continuous line and the 1σ variations are shown as dotted lines. Slope values are $c = -1.33 \pm 0.15$ for DR 21 (E) and $c = -0.92 \pm 0.15$ for DR 21 (W).

TABLE 1

POWER-LAW RELATIONS IN THE DR 21 OUTFLOW

DR 21 (E)		DR 21 (W)	
Flux – Velocity: $dF/dv \propto v^\gamma$			
γ	$\log(v_{break})$	γ	$\log(v_{break})$
2.7±0.6	1.00±0.03	3.5±0.9	1.35±0.03
Velocity Dispersion – Clump Size: $\sigma_v \propto R^a$			
$a = 0.31 \pm 0.11$		$a = 0.62 \pm 0.16$	
Velocity Dispersion – Intensity: $\sigma_v \propto I^c$			
$c = -1.33 \pm 0.15$		$c = -0.92 \pm 0.15$	
Density – Size: $n \propto R^b$			
$b = -0.92 \pm 0.19$		$b = -1.05 \pm 0.22$	

8. CONCLUSIONS

We present near-IR scanning Fabry-Pérot velocity cubes with a spectral resolution of 24 km s⁻¹ of the H₂ v=1-0 S(1) 2.12 μm emission in the entire DR 21 outflow, covering a region of $7.0' \times 4.6'$(5.1 pc $\times$ 3.4 pc at a distance D = 2.5 kpc). The outflow extends on the sky $\sim$6.5′ ($\sim$4.7 pc). We detected H₂ emission from both the DR 21 (E) and DR 21 (W) lobes in a wide velocity interval (-80.82, $+46.84$) km s⁻¹. Velocity maps show an extremely clumpy and complex structure. The most conspicu-

ous sources include a jet-like (region A) and a bow-like (B) in the eastern lobe, designated DR 21 (E):A and DR 21 (E):B; and four regions in the western lobe, a complex cloud C, DR 21 (W):C, near the exciting source and bow-like clouds D, E, and F, designated DR 21 (W):D, DR 21 (W):E and DR 21 (W):F.

The outflow kinematics show: (a) A bimodal radial velocity distribution with peak velocities of $+10$ km s⁻¹ and -17 km s⁻¹; the reddest component arises mainly from clouds E and F, and DR 21 (E)

shows a single peak at velocity -10 km s^{-1} which extends asymmetrically towards the red. (b) The position-velocity diagrams show that v_r in DR 21 (E) appears dominated by a gradient from $+5$ km s^{-1} to -15 km s^{-1}, as if it were accelerating (Hubble flow), followed by a steeper deceleration. In DR 21 (W) we note two different systems: first, cloud D with a wide range of blue velocities from -10 to -35 km s^{-1}, and second, the outflow abruptly becomes red-shifted and bows E and F have velocities around $+8$ and $+5$ km s^{-1}, respectively. (c) The four velocity moments (intensity, centroid velocity, velocity dispersion and kurtosis) are calculated and studied along the outflow assuming that the center is located at the position of the HCO$^+$ peak and that the outflow has a PA=66°; peaks in intensity corresponding to clouds A, B, D, E and F are detected. Velocity gradients in DR 21 (E) from $+13$ to -20 km s^{-1} were detected, while DR 21 (W) shows blue-shifted emission for cloud D followed by the red-shifted bows E and F possibly due to increasing turbulence upstream in the outflow. The kurtosis values are close to zero favoring mostly symmetrical profiles within the slit regions.

We note that the two inner bows, B on the east and D on the west seem to describe the edges of an elliptical cavity. However, the western edge is bluer indicating a possible inclination effect. The major and minor axes of this cavity are 1.8 pc and 0.8 pc, respectively. Inside the cavity the detection of H$_2$ is limited to a few small low surface brightness clumps near structure C (which we argue is a reflection nebulosity, not a shocked region), so most of the H$_2$ gas inside the cavity has been swept out by the outflow.

The color-coded Doppler images of the region allow us to identify a blue jet-like structure that lies at the center of the bow B but moves faster. We propose that this is indeed a jet based on the following arguments: (i) It has a filamentary structure extending for at least 64″(0.73 pc at 2.5 kpc) with a width of 6″. (ii) The kinematics of the jet is quite different from that of the surrounding cloud (B), $v_j = -18 \pm 5$ km s^{-1} while $v_B = -9 \pm 5$ km s^{-1}. (iii) The jet is well aligned with the outflow driving source and with the eastern tip of the outflow (A). (iv) The jet speed is the fastest region found in DR 21 (E). (v) The jet is centered inside the cavity described by region B. In DR 21 (W) we note a quite faint structure that could be the counter-jet to the south of the structures D and E. Arguments in favor of a counter-jet are: (i) it is roughly aligned with the eastern jet; (ii) it is aligned with the driving source and with the apices of bow structures E

and F; (iii) $v_{cj} = -25 \pm 7$ km s^{-1} $< v_{E,F}$ ($+5\pm5$ and 0 ± 5 km s^{-1}, respectively). But the counter-jet is bluer than the jet by 10 km s^{-1} and should be redder, suggesting that it may be an independent jet.

The location and identification of the outflow central source is still uncertain. The presence of the internal jet-like blue-shifted structure in the eastern lobe described above, as well as the possible counter-jet, strongly favor the position of the HCO$^+$ molecular peak (Garden & Carlstrom 1992).

Using the Clump Find algorithm presented by Williams et al. (1994) to locate 3-D coherent structures (clumps) in the data cubes, we were able to detect $\sim$200 clumps in each of the outflow lobes. By spatial averaging, representative values of the velocity moments in each clump were used to study velocity moments and clump area along the outflow lobes. The clump areas rise from one edge, reach a maximum at the bows and decline at the other edge. Small clumps are evident at all positions along the outflow lobes. The clump velocity moments are consistent with the outflow velocity moments results described above. The velocity dispersion within each clump, σ_v shows no strong variation with position along the outflow, and has a mean value of $\sim 5 \pm 3$ km s^{-1} for DR 21 (E) and a slightly higher value 6 ± 3 for DR 21 (W).

Finally, we discuss four power-law relations, between kinematic parameters (flux, velocity) and clump properties (size, intensity, velocity dispersion, density) of the DR 21 outflow.

(a) Flux-velocity relation: Salas & Cruz-González (2002) showed that several outflows have a flat spectrum for low velocities followed by a power-law decrease $dF/dv \propto v^\gamma$ above a certain break velocity. The power-law index is very similar for different outflows, as is the case for DR 21 (E) and DR 21 (W), in which γ is 2.7$\pm$0.6 and 3.5$\pm$0.9, respectively. However, the break velocity is slightly different: $\log(v_{break})$ (in km s^{-1}) takes values of 1.00$\pm$0.03 and 1.35$\pm$0.03, respectively.

(b) Clump velocity dispersion vs. characteristic clump length: A power-law $\sigma_v \propto R^a$ is obtained and compared to Larson's First Law (a=0.38; Larson 1981), Kolmogorov turbulence (a=0.33) and virialized gas (a=0.5). Considering all the clumps in each lobe the correlation is weak but for individual clouds the correlation improves. Cloud B in DR 21 (E) shows a spectral index of a =0.31$\pm$0.11, while for cloud D in DR 21 (W) a=0.62$\pm$0.16. This last result indicates that the eastern outflow is most likely fully turbulent while the western one seems more

virialized. Thus, we present evidence that supports a differentiated kinematics for each lobe.

(c) Velocity dispersion – intensity: A power-law $\sigma_v \propto I^c$ is obtained where large σ_v values correspond to fainter sources. DR 21 (E) shows that a steep $c = -1.33 \pm 0.15$ describes the variation, while a shallower slope $c = -0.92 \pm 0.15$ is found in DR 21 (W).

(d) Density – size: $n \propto R^b$ is the second Larson's law with $b \approx -1.1$ for molecular clouds. We show that $b = a(1 + 1/c) - 1$ and obtain that b is -0.92 ± 0.19 for DR 21 (E) and -1.05 ± 0.22 for DR 21 (W), respectively. We conclude that both lobes yield b values quite consistent with Larson's second law value b of -1.1 and close to the virial equilibrium value of -1.

REFERENCES

Campbell, M. F., Niles, D., Nawfel, R., Hawrylycz, M., Hoffmann, W. F., & Thronson, H. A., Jr. 1982, ApJ, 261, 550

Colomé, C., Harvey, P. M., Lester, D. F., Campbell, M. F., & Butner, H. M. 1995, ApJ, 447, 236

Cruz-González, I., et al. 1994, RevMexAA, 29, 197

Cyganowski, C. J., Reid, M. J., Fish, V. L., & Ho, P. T. P. 2003, ApJ, 596, 344

Davis, C. J., & Smith, M. D. 1996, A&A, 310, 961

Dickel, J. R., Dickel, H. R., & Wilson, W. J. 1978, ApJ, 223, 840

Dickel, H. R., Goss, W. M., Rots, A. H., & Blount, H. M. 1986, A&A, 162, 221

Fischer, J., Sanders, D. B., Simon, M., & Solomon, P. M. 1985, ApJ, 293, 508

Garden, R. P., & Carlstrom, J. E. 1992, ApJ, 392, 602

Garden, R. P., Geballe, T. R., Gatley, I., & Nadeau, D. 1986, MNRAS, 220, 203

_____. 1991a, ApJ, 366, 474

Garden, R. P., Hayashi, M., Hasegawa, T., Gatley, I., & Kaifu, N. 1991b, ApJ, 374, 540

Genzel, R., & Downes, D. 1977, A&AS, 30, 145

Goodman, A. A., Barranco, J. A., Wilner, D. J., & Heyer, M. H. 1998, ApJ, 504, 223

Harris, S. 1973, MNRAS, 162, 5P

Hiriart, D., Salas, L., & Cruz-González, I. 2004, AJ, 128, 2917

Larson, R. B. 1981, MNRAS, 194, 809

Marston, A. P., et al. 2004, ApJS, 154, 333

Riera, A., Raga, A. C., Reipurth, B., Amram, P., Boulesteix, J., Cantó, J., & Toledano, O. 2003, AJ, 126, 327

Roberts, D. A., Dickel, H. R., & Goss, W. M. 1997, ApJ, 476, 209

Salas, L., & Cruz-González, I. 2002, ApJ, 572, 227

Salas, L., et al. 1999, ApJ, 511, 822

Williams, J. P., de Geus, E. J., & Blitz, L. 1994, ApJ, 428, 693

Wilson, T. L., & Mauersberger, R. 1990, A&A, 239, 305

Wilson, T. L., Gaume, R. A., Johnston, K. J., & Tieftrunk, A. R. 1995, ApJ, 452, 693

Yu, K. C., Billawala, Y., & Bally, J. 1999, AJ, 118, 2940

Irene Cruz-González: Instituto de Astronomía, Universidad Nacional Autónoma de México, Apdo. Postal 70-264, México, D. F. 04510, México (irene@astroscu.unam.mx).

Luis Salas and David Hiriart: Instituto de Astronomía, Universidad Nacional Autónoma de México, Apdo. Postal 877, Ensenada, B. C. 22830, México (salas, hiriart@astrosen.unam.mx).